Nanoscale

ARTICLE

Carriers Transport in Quantum Dot Quantum Well Microstructures of Self-assembled CdTe/CdS/ligand Core-shell System

K. Y. Li, [a,†] Q. S. Shan, [a] R. P. Zhu, [a] H. Yin, [a] Y. Y. Lin, [a] L. Q. Wang [b]

Abstract The study on quantum dot quantum well (QDQW)' microstructure modified by choosing different ligand containing a sulfhydryl group is of significant because it enables to regulate photoexcited free charge carries' (FCCs') transport behaviours in high-quality CdTe/ligand QDs via self-assembled way. The photoelectron characteristics of ligand-capped CdTe nanoparticles were probed by a combination of surface photovoltaic (SPV) and photoacoustic technologies, supplemented by a computer simulation method of the CASTEP module. The experiment reveals that D-value ΔE_{Wi} obtained by associated two parameters of the SPV spectroscopy was closely related to the quantum confinement energy in the self-assembled CdTe/CdS/ligand core-shell system. In the paper the D-value was called the depth of QWs, which were buried in the space charge regions located in the graded-band-gap and at either side of the shell-CdS. Obvious resonance quantum tunnelling may occur in the energy band structure with deep QWs at using certain ligand, resulting in extended diffusion length of the FCCs at illumination of the photon energy $h\upsilon \geq E_{g, core-CdTe}$, and in strong SPV response at specific wavelength region. In addition, the carrier—longitudinal optical phonon interaction is the reciprocal of the carriers' lifetime. The d-frontier orbital in the graded-band-gap plays an important role in both the microstructure and the resonance quantum tunnelling of the QDQWs system according to the CASTEP calculations.

1. Introduction

In the last decade, there has been a steady increase in theoretical research and experimental work on various core-shell structure semiconductor nanocrystals, which may make up a quantum dot quantum well (QDQW) nanostructure. This has been carried out by means of theory and experiment methods such as the finite element method[1], linear and branched topology[2], and photoluminescence[3-6]. The interest in these nanostructures is due to their unique electrical, optical, and transport characteristics as compared with conventional materials, even two- and one-dimensional nanomaterials[7-13]. The concept of QDQWs originated with Esaki and Tsu[14], who established the ideas of super-lattices and quantum wells (QW) in semiconductor heterostructures. Following in their footsteps, it was found that the electron levels and resonance quantum tunnel effect of the QWs that were buried in super-lattice structures have the potential for widespread use in the fields of advanced generation photoelectronic and microelectronic devices[15-19]. Research into one particular high-quality quantum dot (QD) consisting of II/VI semiconductors, a ligand-stabilized CdTe QD, has recently excited

interest because of the quantum confinement effect, and because of its widespread use as biomarkers, luminescent materials, and photon crystals[20-25]. Research into the QDs has mainly focused on synthetic methods, morphology, electronic and optical properties[26-29, 30]. The study of QDQW's microstructures in the self-assembled CdTe/CdS/ligand nanostructure, however, has rarely been reported so far. In our previous studies[31, 32], a combination of surface photovoltaic (SPV) and photoacoustic (PA) techniques have been used to probe the characteristic charge transfer (CT) transition channels on the surfaces and at buried interfaces for different ligand-capped crystalline CdTe nanoparticles, and to explore the microdynamic behaviour of the photo-generated free charge carriers (FCCs) of high-quality CdTe/ligand self-assembled QDs. This behaviour is closely related to the energy transformation among specific quantum states, such as the electron and vibration levels of an elementary reaction. In addition, it was experimentally detected by the techniques that two QWs could be identified at two given wavelengths in buried interfacial space charge regions (SCRs) of CdTe/CdS/ligand nanoparticles with a core–shell structure. It was also established that this was because of a quantum tunnel effect, resulting in an antipodal transient photovoltaic response polarity for the CdTe nanocrystals capped respectively by two different ligands.

In order to carry out a microscopic study of possible mechanisms for the QDQWs' microstructure that is formed in between the ligand and the CdTe nanoparticles in terms of the self-assembled core-shell nanostructure, in the present paper, the transport characteristics of the photo-generated FCC's and the electronic structure in CdTe nanoparticles capped by various ligands were studied by both experimental and theoretical methods (*i.e.* using a combination of the SPV and the PA techniques supplemented by a computer simulation method of the CASTEP module).
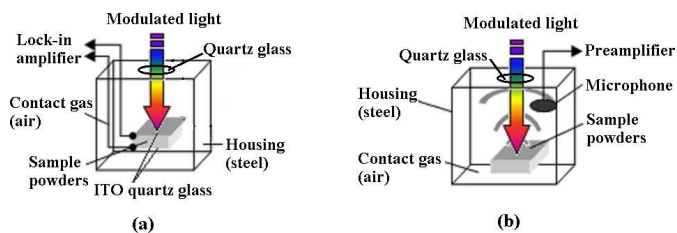
2. Experimental

2.1 Sample preparation

CdTe nanocrystals were prepared according to a previously published method for aqueous synthesis at room temperature[33, 34]. Briefly, freshly prepared NaHTe solution was injected into a solution of $CdCl_2$ and 3-mercaptopropionic acid (MPA) (β-mercaptoethylamine (MA), thioglycolic acid (TGA), or 1-thioglycerol (TG)) which was degassed with N_2 for 30 min at pH 9.5. The concentration of $CdCl_2$ was 1.25×10^{-3} mol/L and the Cd^{2+}/MPA (MA, TGA, or TG)/Te^{2-} molar ratio was 1:2.4:0.2. The crude solution was refluxed at 100 °C for 10 h to obtain CdTe nanocrystals. The number of CdTe nanocrystals in solution was calculated as 10^{-5}-10^{-6} mol/L.

The samples prepared were denoted as MPA-r, MA-r, TGA-r, and TG-r, where MPA (MA, TGA, or TG) -r indicated MPA (MA, TGA, or TG) -capped CdTe nanoparticles with an average particle size of 4.0 nm (red) at a Cd^{2+} concentration of 0.01 M. High-resolution transmission electron micrographs (HRTEM) and fast Fourier transform (FFT) were recorded on a JEOL-2010 electron microscope (Japan) operating at 200 kV. Fourier transform infrared spectroscopy (FTIR) was recorded on a Bruker EQUINOX55 FTIR (Germany).

All optical measurements were performed at room temperature under ambient conditions.

2.2 Surface photovoltaic and photoacoustic spectroscopy

SCHEME 1. Schematic depiction of the experimental setup for measurement of both surface photovoltaic (SPV) spectroscopy (a) and photoacoustic (PA) spectroscopy (b). In order to achieve the same probe environment for both SPV and PA measurements, the experimental parameters in the setup were kept the same, despite exchanging the sample cells.

The principles and experimental details of SPV spectroscopy have been described elsewhere[35, 36]. Schemes 1a and 1b show our setup for SPV and PA spectroscopy, respectively. The detection device

and the conditions of the two tests were the same except for exchanging the sample cells. The experiment irradiation was a 500 W Xe-arc lamp. The PA spectroscopy of the samples was normalized by the PA signals of carbon black powders. PA spectroscopic analysis was firstly conducted under different modulation frequencies, ranging from 20 to 80 Hz, to confirm the detected PA signals only from surfaces and phase interfaces of the samples prepared. And the low modulation frequency of 22 Hz was adopted in the test process.

SPV and PA technologies can also be used effectively to obtain information on photoelectron behaviours at phase interfaces, because the techniques are by no means sensitive only to surfaces. Rather, they are sensitive to the entire surface SCRs by super- or sub-bandgap absorption, and even to buried interfaces located anywhere in the sample, as long as they can be reached by photons[35].

3. Experimental results and discussion

3.1 Clarification of a core-shell microstructure of ligand-capped CdTe nanoparticles

The HRTEM of the sample MPA-r are shown in Fig.1a: The average grain size of the sample was about 2.9 nm. The interplanar spacings of three selected nanocrystalline grains were 0.34 nm. This value was between the interplanar spacings of the (111) planes of the CdTe and CdS lattices. However, the cell parameter was closer to that of CdTe with a sphalerite structure according to the electron diffraction pattern and the indexing analysis, and X-ray diffraction curve (SI Figs.1 and 2). This implied that a distortion of the lattice cell occurred because sulfur atoms in the ligand MPA partially replaced tellurium atoms located at the surfaces and the boundary of CdTe nanoparticles. Energy-dispersive X-ray spectroscopy (EDS) of the samples MPA-r and TGA-r (Figs. 1b and 1c) also indicated that the samples consisted essentially of Cd, Te, and S elements, resulting from the -HS group in the ligands coordinating with CdTe nanoparticles, *i.e.*, the S atoms in the group may partially replace Te atoms located on the surface and grain boundary of CdTe nanoparticles, and then form a CdS layer capped on the surface of the nanoparticles. In addition, the relative contents of S atoms and Cd or Te atoms in the MPA sample were about twice that in the TGA sample as seen in Figs. 1b and 1c.
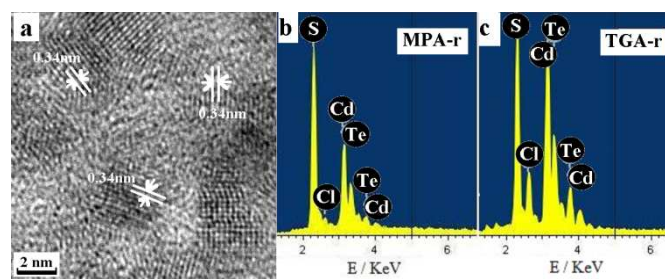

FIG. 1. High-resolution transmission electron micrographs and fast Fourier transform of the sample MPA-r (a); energy dispersive X-ray spectra of MPA (b) and TGA (c)-capped CdTe nanoparticles.

Fig. 2a shows the FTIR spectra of the samples MPA-r, MA-r, TGA-r, and TG-r. According to a spectra library the broad and strong absorption peak at 3394 cm^{-1} was assigned to the -OH vibration at alkyl chains in some ligand, υ_{-OH}. For MPA- and TGA- stabilized CdTe nanoparticles, two narrow absorption peaks at 1386 and 1590 cm^{-1} were assigned to the COO- stretching vibration, υ_{COO-}, and the C=O stretching vibration, $\upsilon_{C=O}$, respectively. It is significant that the absorption peak that was associated with the S-H stretching vibration, υ_{S-H}, disappeared at 2550 cm^{-1} for all four samples. And at the same time the C-S stretching vibration, υ_{C-S}, should have appeared at 654cm^{-1}, but moved to high frequency with 663cm^{-1} because of the effect of Cd-S coordination bond. This implied that the S-H bond in those ligands had been broken, and that then the Cd-S bond may be made in the self-assembly process of the core-shell structural nanoparticles. These inferences were consistent with the HRTEM and EDS results of the samples MPA-r and TGA-r shown in Fig. 1. Consequently, self-assembled core-shell structures of the four samples may be formed. More specifically, it can be assumed that that the core of the core-shell microstructure is a CdTe nanocrystal with an average grain size of about 2.9 nm. The external surface of the grain may be capped by the cluster of some ligand that was incorporated in the CdTe$_{1-x}$S$_x$ ($0 \leq x \leq 1$) nano-particle by breaking the S-H bond and making the Cd-S bond, i.e. a shell-CdS was located at between the core-CdTe and ligand, and the thickness of the shell may be about monomolecular layer.
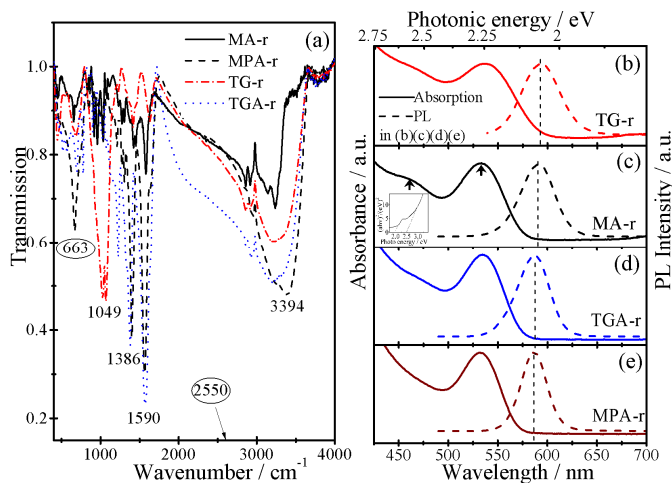

FIG. 2. Fourier transform infrared spectra of the samples MPA-r, MA-r, TGA-r, and TG-r (a), UV-VIS absorption and fluorescence spectra of the samples TG -r (b), MA-r (c), TGA-r (d), and MPA –r (e). The inset in (c) is the optical band gaps of the core-CdTe and the shell-CdS of the MA-r obtained by Tauch-Menth extrapolation, which are listed in Table 1.

The absorption curve in Fig. 2c displays that two optical band-gaps of the sample MA-r were respectively located at about 2.3 eV (λ_1, 539 nm) and 2.7 eV (a small shoulder peak, λ_2=459 nm), the former related to the core-CdTe absorption transition, the latter to the shell-CdS absorption transition, which agreed with Ref. 30. However, the shoulder peak of other three samples was very obscure, even was unrecognized. This may be because the shell-CdS of them

was too thin to show the adsorption at 459 nm in Figs. 2b, 2d, and 2e. The average grain size D$_{UV-VIS}$ of the samples was calculated according to Ref. 37 and given in Table 1, which was agreement with the result of the HRTEM in Fig. 1a. Because the average grain sizes of the prepared CdTe QDs were much smaller than the exciton Bohr radius of CdTe, a$_B$ = 5.17 nm (Eq. 1), the optical transition energy of the samples can be estimated by the so-called nanocrystal strong confinement effect[38]. Here, the lowest excited state energy (LESE) E (D) is obtained by Eq. 2, in which the second term is quantum confinement energy ΔE_g (Eq. 3),

$$a_B = \frac{0.053\varepsilon}{m^*/m_0} \tag{1}$$

$$E_{g,UV-VIS} = E(D) = E_g + \frac{\hbar^2}{2m^*} \cdot \frac{\pi^2}{D_{UV-VIS}^2} \tag{2}$$

$$\Delta E_g = \frac{\hbar^2}{2m^*} \cdot \frac{\pi^2}{D_{UV-VIS}^2} \tag{3}$$

Where, in Eq. 1 ε is the permittivity; m* exciton reduced mass; and m$_0$ electron rest mass. In Eq. 2 E$_{g-UV-VIS}$ is optical band gap obtained by UV-VIS absorption spectra of the samples; E$_g$ is the band gap of bulk material at 300 K (E$_{g, CdTe}$ = 1.49 eV). The effective masses of electrons and holes of CdTe, m$_e$* and m$_h$*, are 0.12 m$_0$ and 0.48 m$_0$, respectively[39]. The results obtained by above equations are listed in Table 1.

On the other hand, fluorescence wavelengths that were respectively emitted by the four samples were from 585 nm (TG-r), 583 nm (MA-r), 582 nm (TGA-r), to 580 nm (MPA-r), i.e., there was a blue shift phenomenon of the PL intensity at using different ligand in terms of the four samples. And the wavelength range of emitted fluorescence of the sample MPA-r was narrower than that of other three samples as the photoluminescence curves shown in Figs. 2b, 2c, 2d, and 2e. Obviously, the differences of the UV-VIS absorption spectra and PL spectra in Figs. 2b-e between the four samples should be related to their respective electron structure in the core-shell microstructure system mentioned above.

3.2 Analysis of surface photovoltaic and photoacoustic spectroscopy

The SPV spectra of the samples MPA-r, MA-r, TGA-r, and TG-r are shown in Figs. 3a$_1$, 3b$_1$, 3c$_1$, and 3d$_1$, respectively. In the SPV spectra of all four samples, there appeared three SPV response peaks, knee$_1$, knee$_2$, and knee$_3$, and two valleys, QW$_1$ and QW$_2$, in the wavelength range of UV-NIR light. It is interesting that, however, the four samples varied from one another in both the intensity of the SPV response and the photon energy resulting in the CT transitions, corresponding to these peaks and valleys in Figs. 3a$_1$, 3b$_1$, 3c$_1$, and 3d$_1$. Obviously, these were caused by the different ligands used. In our previous reports[31], the three SPV response peaks related to the knee$_1$, knee$_2$, and knee$_3$ were assigned to the photo-generated FCC's transfer transitions, and were connected with the optical bandgaps of E$_{g, core-CdTe, SPV}$, E$_{g, shell-CdS, SPV}$, and E$_{g, outer-layer-}$

ligand, SPV, respectively, according to the abscissa of the largest external tangent of the band, the calculated photoelectric thresholds of the SPV responses. Interestingly, the knee$_2$ of the four samples in Figs. 3a$_1$-d$_1$, which connected with the photoelectric threshold of E$_{g,}$ $_{shell-CdS,\ SPV}$, was more obvious than the shoulder peak of the absorption curves at 459 nm in Figs. 2b-e, because the sensitivity of SPV detection technology is several orders of magnitude higher than some standard electron spectra such as XPS and Auger electron spectrum [35].
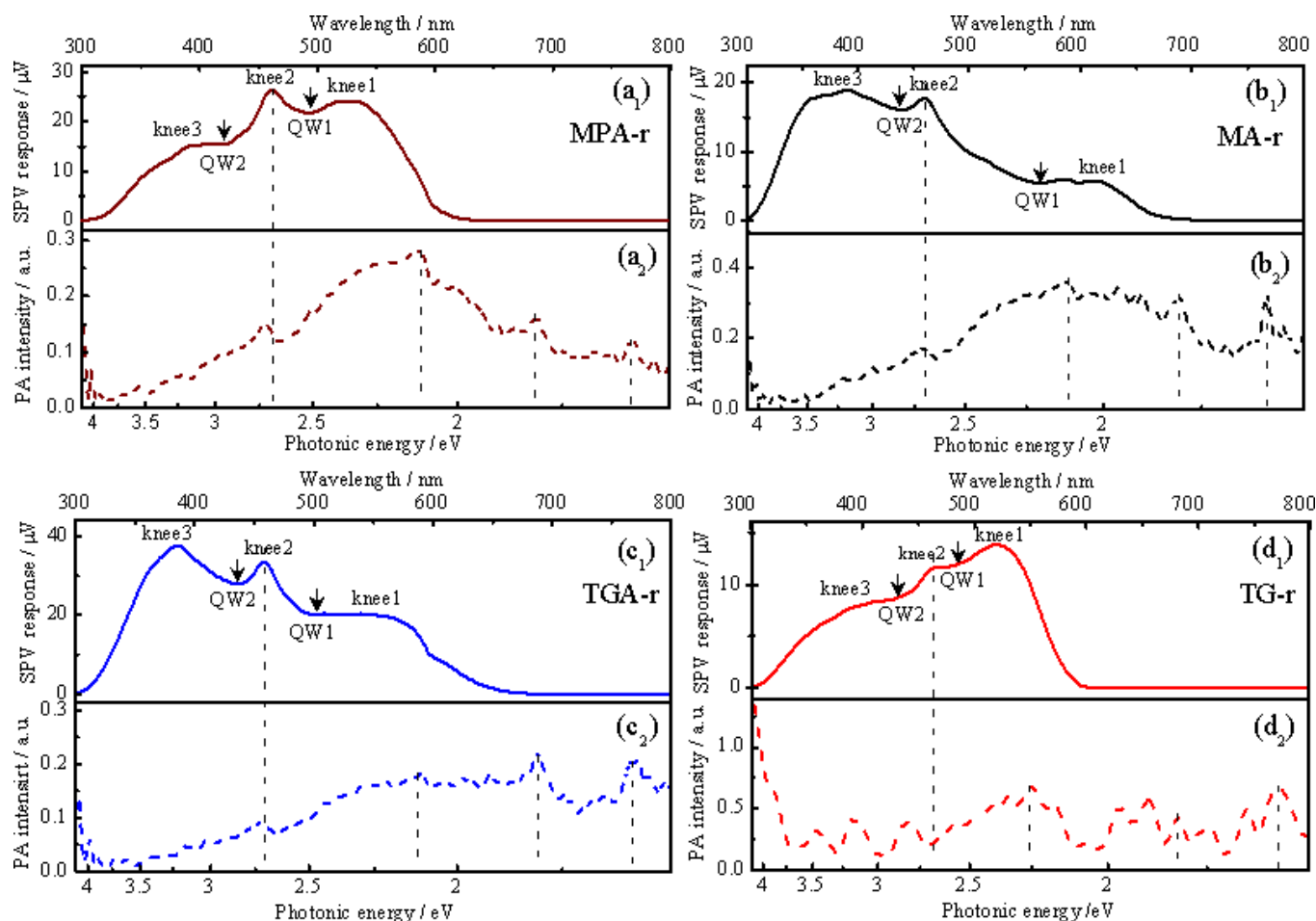

FIG. 3. Surface photovoltaic spectra of the samples MPA-r (a$_1$), MA-r (b$_1$), TGA-r (c$_1$), and TG-r (d$_1$), Photoacoustic spectra of the samples MPA-r (a$_2$), MA-r (b$_2$), TGA-r (c$_2$), and TG-r (d$_2$).

These photoelectric thresholds are listed in Table. 1, in which the numerical values of E$_{g,\ core-CdTe,\ SPV}$ were a good agreement with that of E$_{g,\ \lambda1,\ UV-VIS}$, except the E$_{g,\ shell-CdS,SPV}$ values were slightly smaller than the E$_{g,\ \lambda2,\ UV-VIS}$ values for the MA-r, and the E$_{g,\ shell-CdS,SPV}$ values of the four samples were equal to each other.

The two valleys (QW$_1$ and QW$_2$) of the SPV response of the four samples in Figs 3a$_1$, 3b$_1$, 3c$_1$, and 3d$_1$ were attributed to the photo-generated CT transitions in connection with the two quantum wall structures QW$_1$ and QW$_2$, which were respectively located in the interface SCR$_1$ between the core-CdTe and the shell-CdS, and SCR$_2$ between the shell-CdS and some ligand of the ligand-capped CdTe microstructure as indicated in Fig. 4a. This was because in between those three 'knees', the shape of the SPV spectrum resembles (an inverted) typical absorption spectra of multi-quantum-well (MQW)

structure[40]. The photon energies associated with the two QWs in Figs. 3a$_1$, 3b$_1$, 3c$_1$, and 3d$_1$ were denoted as E$_{QW1}$ and E$_{QW2}$, respectively. The numerical values of these energies of the four samples are listed in Table 1. Here, the difference between the photon energy related to a certain QW and the photoelectric threshold of the peak closest to the QW on long wavelength side of SPV spectroscopy is defined as ΔE$_{Wi}$, that is,

$$\Delta E_{Wi} = E_{Vi} - E_{g,Pi,SPV} \qquad (4)$$

where subscripts $_{W,\ V,\ P}$, and $_i$ represent well, valley, peak, and label corresponding to specific SPV response, respectively. As compared ΔE$_{Wi}$ with corresponding ΔE$_{g,\ \lambda i}$ values of the four samples in Table 1, it is found that the values were almost identical to ΔE$_{W1}$ and ΔE$_{g,}$ $_{\lambda1}$, except the ΔE$_{W2}$ was slightly bigger than the ΔE$_{g,\ \lambda2}$ in terms of a certain sample. Obviously, ΔE$_{Wi}$ obtained by the parameters of the

SPV spectroscopy was closely related to the quantum confinement energy in prepared self-assembled CdTe/CdS/ligand core-shell structural nanoparticles. This confirmed that some quantum well structures existed in the quantum dots system. Consequently, ΔE_{Wi} was called quantum well depth. Furthermore, the properties of the ligands may directly affect the depth of the QWs and the photo-generated FCCs' transport behaviours in the system as shown in Fig. 3. The graded-band-gap scheme of prepared CdTe/CdS/ligand core-shell system at illuminated by UV-NIR light is illustrated in Fig. 4b, according to the above results and to the numerical value of the photon energies that were related to the knees and valleys of the SPS of the four samples in Figs. 3a$_1$, 3b$_1$, 3c$_1$, and 3d$_1$, respectively.
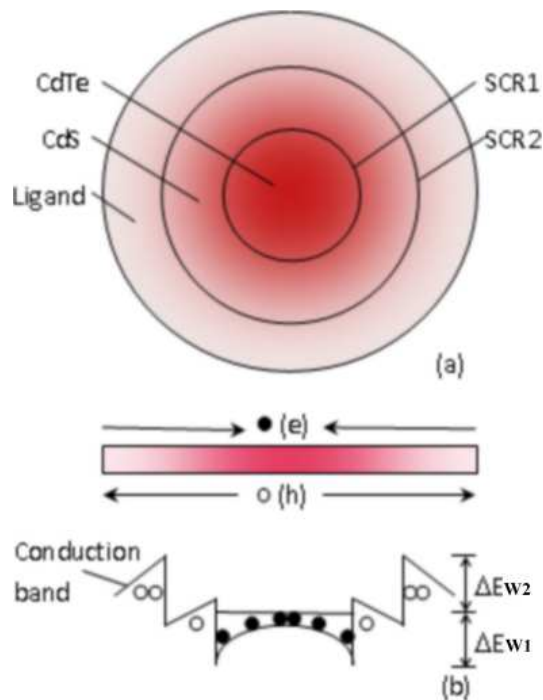

FIG. 4. Core-shell microstructure scheme models (a) and graded-band-gap of self-assembled CdTe/CdS/ligand core-shell structure (b) at illumination of UV-NIR light. The ΔE_{W1} and ΔE_{W2} values calculated by Eq. 4 refer to Table 1.

In comparing the $\Delta E_{W1\ or\ 2}$ values of the four samples in Table 1, an interesting order can be seen: $\Delta E_{W1\ or\ 2,\ MPA-r} > \Delta E_{W1\ or\ 2,\ TG-r} > \Delta E_{W1\ or\ 2,\ TGA-r} > \Delta E_{W1\ or\ 2,\ MA-r}$. According to the literature[41, 42] the QWs in a semiconductor heterostructure may result in resonance quantum tunneling in its energy band, and the deeper the QWs, the more obvious is the resonance quantum tunneling, when the width of the QWs is so thin as to cause a strong coupling between the QWs. If we do not think resonance quantum tunneling in the core-shell microstructure system, the situation can be that the FCCs carrying with negative charge in a sample, which were induced by illumination with the photon energy $h\upsilon \geq E_{g,\ outer-layer-ligand}$, moved from the outer-layer-ligand to the core-CdTe; the holes may be partially trapped in the QW$_1$ and QW$_2$ that were located at the interfaces SCR$_1$ and SCR$_2$, respectively, because the electron affinity of the core-CdTe was greater than that of the shell-CdS and the outer-layer-ligand as shown in Fig. 4b. This may result in the SPV

response that was related to the ligand at the shortwave region was stronger than other two that were connected with the shell-CdS and the core-CdTe at illumination with the photon energy $h\upsilon \geq E_{g,\ outer-layer-ligand}$. The SPV spectroscopes of the samples MA-r and TGA-r in Figs. 3b$_1$ and 3c$_1$ belonged to the above case. On the contrary, the intensity of knee$_1$ in Figs. 3a$_1$ and 3d$_1$ of the samples MPA-r and TG-r, which was related to the SPV response of the core-CdTe, exceed over that of knee$_3$ that is connected with the SPV response of the ligand. This may result from stronger resonance quantum tunneling of the two samples as compared with the MA and TGA samples, which leaded to movement of the photo-generation FCCs carrying with negative charge from the core-CdTe to the outer-layer-ligand, and to prolonged lifetime of the FCCs at illumination of the photon energy $h\upsilon \geq E_{g,\ core-CdTe}$. In other words, obvious resonance quantum tunneling should contribute to increase in those photo-generated FCCs' diffusion lengths upon illuminated by the photon energy $h\upsilon \geq E_{g,\ core-CdTe}$, and to enhance the SPV characteristics of the core-CdTe in the core-shell structure nanoparticles, because of the fact that the potential well depths $\Delta E_{W1\ or\ 2,\ MPA}$ and $\Delta E_{W1\ or\ 2,\ TG}$ of the samples MPA-r and TG-r were deeper than that of the samples MA-r and TGA-r. This inference was a good agreement with the blue shift phenomenon of the PL intensity of the four samples in Figs. 2b-2e. The experimental results above prove these theoretical deductions[43]. Furthermore, considering the possible core-shell structure of the four samples, the coordinate bond may be formed between the lone-pair electrons of the carbonyl or amido group at the alkyl chain of some ligand and the unoccupied s-orbital of the Cd^{2+} ions located at the surface of CdTe nanoparticles. At the same time the S atom in -HS group of the ligands may partially replace the Te atom in CdTe, and then form a CdS layer capped on the surface of CdTe nanoparticles. Other unbonded lone-pair electrons in the ligand, such as that in amido groups of the ligand MA and in hydroxyl groups of the ligand TGA, can be excited to the π antibonding orbital of the ligand upon illumination by photon energy $h\upsilon \geq E_{g,\ outer-layer-ligand}$, which is the so-called n-π^* transition that is defined as the transition of electrons from a nonbonding orbital to an antibonding π orbital. The n-π^* transition occurring within the ligand may have an inhibiting effect on resonance quantum tunnelling, i.e., the n-π^* transition may play a competitive inhibition in the photo-generated negative FCCs transferring from the core-CdTe to the outer-layer-ligand, resulting in a smaller electron affinity of the outer shell layer of the samples MA-r and TGA-r as compared with the samples MPA-r and TG-r. This was confirmed by the results of the electric field induced SPS of the MPA-r (see SI Figs. 3a and 3b). Consequently, the ligand covering the CdTe nanoparticles not only acts a stabilizing agent, but may to a certain extent control the transport behaviour of the photo-generated FCCs in the QDQWs microstructure. Another interesting phenomenon was that the photoelectric thresholds $E_{g,\ shell-CdS,\ SPV}$ of the shell-CdS of all four samples, corresponding to knee$_2$ in Figs. 3a$_1$, 3b$_1$, 3c$_1$, and 3d$_1$, were 2.30 eV as listed in Table 1. This implied that the effect of the ligands on the photoelectric threshold of the shell-CdS in the core-shell microstructure may be negligible, unlike the intensity of the SPV response at the wavelength relating to knee$_2$ in Figs. 3a$_1$, 3b$_1$, 3c$_1$, and 3d$_1$. And the $E_{g,\ shell-CdS,\ SPV}$ value was smaller than the $E_{g,\ \lambda2,\ UV-VIS}$ value for the sample MA in Table 1. This may be attributed to

complex environment in the interface SCRs located on either side of the shell-CdS, and will be further discussed below by a computer simulation method of the CASTEP module.

TABLE 1. The relevant parameters obtained by the results of UV-VIS absorption and surface photovoltaic spectra of the samples.

Relevant parameter[‡]/eV \ Sample	MPA-r	MA-r	TGA-r	TG-r
D_{UV-VIS} / nm	2.73	2.75	2.76	2.80
$E_{g, \lambda1, UV-VIS}$	2.00	1.99 (1.94[♀])	1.99	1.98
$E_{g, \lambda2, UV-VIS}$	-	2.47[♀]	-	-
$\Delta E_{g, \lambda1}$	0.51	0.50	0.49	0.48
$\Delta E_{g, \lambda2}$	-	-	-	-
$E_{g, core-CdTe, SPV}$	2.01	1.86	1.96	2.09
$E_{g, shell-CdS, SPV}$	2.30	2.30	2.30	2.30
$E_{g,outer-layer-ligand,SPV}$	2.67	2.58	2.42	2.52
E_{QW1}	2.51	2.20	2.49	2.54
E_{QW2}	2.92	2.81	2.85	2.86
ΔE_{W1}	0.50	0.34	0.53	0.45
ΔE_{W2}	0.62	0.51	0.55	0.56

According to Quimby[44] the magnitude of the photoacoustic signal mainly depends on the degradation of the optical energy into heat phonons through single- and multi-phonon relaxation, i.e., is closely related to non-radiative de-excitation process. Therefore, the energy complementarity should exist between photoacoustic and surface photovoltaic effect. To explore the lattice vibration caused by non-radiative energy transformation in the de-excitation process upon illumination by UV-NIR light, Figs. $3a_2$, $3b_2$, $3c_2$, and $3d_2$ display the PA spectra of the samples MPA-r, MA-r, TGA-r, and TG-r, respectively. The profiles of the PA spectra of the samples were basically the same, *i.e.,* strong PA signals appeared mainly at $h\upsilon = 2.70$ eV, 2.11eV, 1.81eV, and 1.62 eV in Figs. $3a_2$, $3b_2$, $3c_2$, and $3d_2$, respectively. Firstly, combining the results of the SPV spectra in Figs. $3a_1$, $3b_1$, $3c_1$, and $3d_1$ and the PA spectra in Figs. $3a_2$, $3b_2$, $3c_2$, and $3d_2$ confirms the complementary relationship of energy conversion between photovoltaic and photoacoustic effects in terms of CdTe nanoparticles capped by a ligand. That is, take the MPA-r for sample, the photogenerated FCCs induced by photon energy from 2.11 eV to 4 eV mainly were used to produce surface photovoltage except a few were used for nonradiative transition upon illuminated by $h\upsilon \geq 2.11$ eV and 2.70 eV, but that induced by $h\upsilon \geq 1.81$eV and 1.62eV were used to cause nonradiative deexcitation process as seen in Figs. $3a_1$ and $3a_2$. The situations of other three samples were similar as shown in Figs. $3b_1$-d_1, $3b_2$-d_2. Secondly, the PA signals located at about 2.70 eV and 2.11 eV in

Figs. $3a_2$-d_2 were corresponding to the wavelengths of the SPV responses of the shell-CdS and the core-CdTe of each of the four samples in Figs. $3a_1$-d_1, respectively, as illustrated by the dash lines in Fig. 3. Therefore, the PA signal appearing at 2.70 eV was related to non-radiative transition between the energy bands of the shell-CdS, while the PA signal at 2.11 eV was related to non-radiative transition between the energy bands of the core-CdTe. Stronger PA signal of the samples MPA-r at about 2.70 eV in Figs. $3a_2$ as compared to the samples TGA-r and MA-r may be attributed to obvious resonance quantum tunnelling, because the quantum confinement energy $\Delta E_{g, \lambda2, MPA}$ and the QWs' depth $\Delta E_{W2, MPA}$ of the sample MPA-r were greater than that of the other two samples except for the TG-r as listed in Table 1. The same situation happened in the TG-r because its quantum confinement energy ($\Delta E_{g, \lambda2, TG}$) and QWs' depth ($\Delta E_{W2, TG}$) were next only to the MPA-r. More specifically, the resonance quantum tunneling can guide the electrons, which were excited from the valence band to the conduction band of the core-CdTe when the photon energy $h\upsilon \geq E_{g, core- CdTe}$, to move from the core-CdTe to the outer-layer-ligand of the core-shell microstructure. That is, the electrons could pass through the heterogeneous boundary that is called as the interface SCR_1 in which the QW_1 was buried, and then partially release energy by way of non-radiative energy transformation when the electrons recombined with the holes in the valence band of the shell-CdS, resulting in strong PA signals at the 2.70 eV in Figs. $3a_2$ and $3d_2$.

These findings were a good agreement with the results of the SPV spectra of the samples in Figs. 3a₁-d₁. Finally, the PA signals at low-energy region such as 1.81eV and 1.62 eV in Figs. 3a₂-d₂ may be related to non-radiative transition between the energy band of the core-CdTe (or the shell-CdS) and the surface states located at heterogeneous boundary. Comparing the PL result of the sample TG-r with the other three samples in Fig. 2b, the emitted fluorescence wavelength of the TG-r was longer and the wavelength range was wider. This implied that non-radiative de-excitation processes occurred between the band and the surface state coinciding with the fluorescence-emission of the TG-r at 585 nm in Fig. 2b, because of strong PA signals of the TG sample at 1.81eV and 1.62 eV in Fig.3d₂. The results above reveal that the shell-CdS in between the CdTe nanoparticle and the ligand is too valuable to be neglected in the electron-phonon interaction of the material. The varying electron structure caused by the sulfur-doping in the CdTe lattice cell or at the surface of it was investigated in the computer simulation detailed below.

4. CASTEP computer simulation results

In our previous study[32], the phonon spectra of both CdTe that belongs to the space group F-43M and $CdTe_{1-x}S_x$ (x=0.5) were obtained by the CASTEP computer simulation method. Those results demonstrated that the property of the localized phonon states that might result in PA signals at 500-600 nm and 780 nm depends strongly on the S-doping in CdTe. Furthermore, it was assumed that the longitudinal optical (LO) mode phonon states might correspond to the PA spectra of the samples capped by various ligands at 780 nm. This carrier—LO phonon interaction is the reciprocal of the carriers' lifetime, corresponding to the intensity of the related SPV response of the samples as mentioned above, which may prove the theoretical results[45]. In order to have a greater insight into the electron structure in the ligand-stabilized CdTe QDQW system, Figs. 5A-C show the atomic arrangement of CdTe (111) face, the partial density of states of both the $CdTe_{1-x}S_x$ cell (x = 0, 0.50, 0.75 and 1.0) and the (111) face (x = 0, 0.15, 0.43 and 1.0) obtained by the CASTEP computer simulation method, respectively. According to Ref. 46 the electrons, which are 4d-, 5s-, and 5p-electrons in the cadmium atoms, 4d-, 5s-, and 5p-electrons in the tellurium atoms, and 3s- and 3p-electrons in the sulfur atoms, respectively, participate in the process of the transfer transition of the photo-generated FCCs in terms of ligand-stabilized CdTe nanoparticles. Both the level and density of states for the s-electrons in the valence band decreased with the increasing number of S atoms that partially replaced Te atoms in CdTe cell, as shown in Fig. 5B. In contrast with the situation of the s-electrons, the level of d-electrons in the valence band moved up to the top of the valence band when Te atoms in CdTe cell were gradually replaced by S atoms. This implied that more and more d-electrons participated in the process of the transfer transition of the photo-generated FCCs due to the S-doping in CdTe. In order to explore the change in the surface electron structure with a varying number of surface-binding thiols of the ligands capping the CdTe nanoparticles, Fig. 5C shows the density of states of the CdTe (111) face under different levels of S-doping. Both the density and

variety of states on the CdTe surface dramatically increased as compared to its cell in Fig. 5B. In fact, the location of the d-electron levels moved up to the top of the valence band relative to the reduced level of s-electron states in the valence band, even though the level of d-electrons looks unchanged in Fig. 5C. It is theoretical confirmation that the d-electron levels moved up to the top of the valence band with an increasing number of surface-binding thiols of the ligands capping the CdTe nanoparticles, resulting in much more d-bonding and -antibonding orbitals having a share in the QDQW structure. More specifically, the d-frontier orbital in nanocrystalline CdTe capped by ligands may play an important role in both the QW structure and resonance quantum tunneling in the core-shell microstructure.
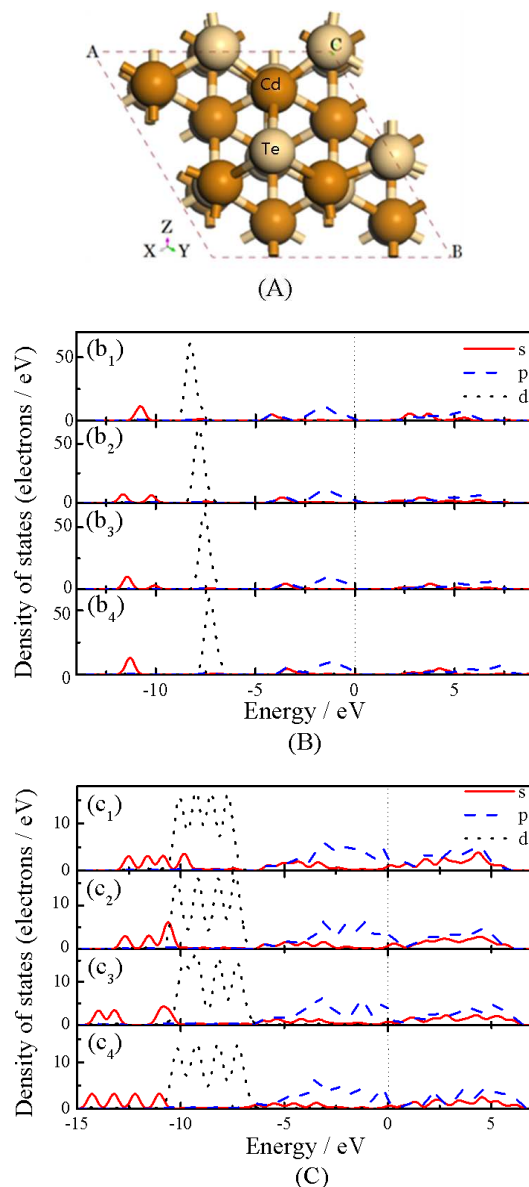

(A)

(B)

(C)

FIG. 5. (A) Atomic arrangement of CdTe (111) face; (B) CASTEP partial density of states of CdTe lattice cell, in which the content of sulfur-doped was 0% (b₁), 50% (b₂), 75% (b₃), 100% (b₄); (C) partial

density of states of CdTe (111) face for the sulfur contents of 0% (c_1), 15% (c_2), 43% (c_3), 100% (c_4).

5. Conclusion

In summary, QDQW's microstructure and photogeneration FCCs' transport behaviours in the self-assembled CdTe/CdS/ligand core-shell system may be probed by a combination of surface photovoltaic and photoacoustic measurements supplemented by the FTIR, the PL, and the UV-VIS absorption spectra, and by a computer simulation method of the CASTEP module. Firstly, the results showed that the ligand-stabilized CdTe nanoparticles possessed both core-shell microstructure and graded-band-gap structural characteristics. More specifically, in the system the FCCs carrying with negative charge may move from the outer-layer-ligand up through the shell-CdS that mainly formed at the (111) plane of CdTe nanoparticles, toward the core-CdTe at illumination with the photon energy $h\upsilon \geq E_{g, \text{outer-layer-ligand}}$, because the electron affinity of the core-CdTe was greater than that of the shell-CdS and the outer-layer-ligand. Secondly, the experiment reveals that ΔE_{Wi} obtained by associated two parameters of the SPV spectroscopy of the sample was closely related to the quantum confinement energy in the self-assembled CdTe/CdS/ligand core-shell structure. Here ΔE_{Wi} was called the depth of quantum wells that were buried in the SCRs located at either side of the shell-CdS. The properties of the ligands may directly affect the depth of the QWs and the photo-generated FCCs' transport behaviours in the QDQWs' microstructure. Obvious resonance quantum tunnelling may occur in the graded-band-gap with deep QWs, such as the situations of the samples MPA-r and TG-r, resulting in movement of the photo-generation FCCs carrying with negative charge from the core-CdTe across the shell-CdS to the outer-layer-ligand, and leading to prolonged lifetime of the FCCs at illumination of the photon energy $h\upsilon \geq E_{g, \text{core-CdTe}}$ and strong SPV response of the samples at specific wavelength region. In addition, the effect of the ligands on the photoelectric threshold of the shell-CdS may be negligible, unlike the intensity of the SPV response at photon energy $h\upsilon \geq E_{g, \text{shell-CdS}}$. Finally, according to the computer simulation results, the density and variety of states on the CdTe (111) face dramatically increased, and the location of the d-electron levels moved up to the top of the valence band relative to the reduced level of s-states in the valence band, with increasing numbers of doped sulfur atoms at the (111) face. This may cause much more d-bonding and d-antibonding orbitals to have a share in the QDQWs' structure. More specifically, the d-frontier orbital in the ligand-capped CdTe core-shell microstructure system may play an important role in both the QDQWs' structure and resonance quantum tunneling.

Acknowledgement

Notes and references

[a] State Key Laboratory of Metastable Materials Manufacture Technology & Science, Yanshan University, Qinhuangdao 066004, China.

[b] Hebei Key Laboratory of Applied Chemistry, College of Environmental and Chemical Engineering, Yanshan University, Qinhuangdao 066004, China.

[†] Author to whom correspondence should be addressed. Electronic mail: kuiyingli@ysu.edu.cn; Telephone: +86 335 8074631

[‡] $E_{g, \lambda1 \text{ (or } \lambda2), \text{ UV-VIS}}$ is the optical band gap obtained by UV-VIS absorption spectra of the samples at $\lambda_1 = 539$ nm (or $\lambda_2 = 459$ nm); $E_{g, \text{core-CdT, SPV}}$, $E_{g, \text{shell-CdS, SPV}}$, and $E_{g, \text{outer-layer-ligand, SPV}}$ represent the photoelectric thresholds of the SPS of the samples at specific wavelength, which were related to the core-CdTe, the shell-CdS, and the outer-layer-ligand, respectively; E_{QW1} and E_{QW2} denote the photon energies associated with the QW_1 and QW_2, respectively; $\Delta E_{W1 \text{ (or W2)}}$ is called the QW_1 (or QW_2) depth in the graded-band-gap and calculated by Eq. 4.

[♀] The optical bandgap of the core-CdTe or the shell-CdS of the MA-r obtained by the inset of Fig.3c.

1 B. Bochorishvili, *Physica E: Low-dimensional Systems and Nanostructures,* 2011, **43**, 874.

2 D. J. Milliron, S. M. Hughes, Y. Cui, L. Manna, J. Li, Lin-Wang Wang, and A. P. Alivisatos, *Nature,* 2004, **430**, 190.

3 P. K. Santra, R. Viswanatha, S. M. Daniels, N. L. Pickett, and J. M. Smith, P. O'Brien, and D. D. Sarma, *J. Am. Chem. Soc.*, 2009, **131**, 470.

4 I. Suárez, H. Gordillo, R. Aborgues, S Albert, and J. Martínez-Paster, *Nanotechnology,* 2011, **22**, 435202.

5 S. Karan, M. Majumder and B. Mallik, *Photochem. Photobiol. Sci.,* 2012, **11**, pp1220-1232.

6 M. Dutta, S. Jana and D. Basak, *ChemPhysChem.*, 2012, **11**, pp1774-1779.

7 B. O. Dabbousi, J. Rodriguez-Viejo, F. V. Mikulec, J. R. Heine, H. Mattoussi, R. Ober, K. F. Jensen, and M. G. Bawendi, *J. Phys. Chem. B*, 1997, **101**, 9463.

8 A. Mews, A. Eychmueller, M. Giersig, D. Schooss, and H. Weller, *J. Phys. Chem.*, 1994, **98**, 934.

9 A. Mews, A. V. Kadavanich, U. Banin, and A. P. Alivisatos, *Phys. Rev. B.* 1996, **53**, 13242.

10 Y. N. Fang, M. Xiao and D. Z. Yao, *Physica E: Low-dimensional Systems and Nanostructures*, 2010, **42**, 2178.

11 A. Merz, J. Siller, R. Schittny, C. Krämmer, H. Kalt and M. Hetterich, *Appl. Phys. Lett.*, 2014, **104**, 252401.

12 M. Ohtsu, K. Kobayashi, T. Kawazoe, S. Sangu, T. Yatsui, *IEEE J. Sel. Top. Quantum Electron.*, 2002, **8**, 839.

13 D. Gammon, E.S. Snow, B.V. Shanabrook, D.S. Katzer, D. Park, *Phys. Rev. Lett.*, 1996, **76**, 3005.

14 L. Esaki and R. Tsu, *IBM Research Note RC-2418*, 1969. *IBM J. Res. Develop.*, 1970, **14**, 61.

15 L. Esaki and L. L. Chang, *Phys. Rev. Lett.*, 1974, **33**, 495.

16 R. Dingle, W. Wiegmannn, and C. H. Herny, *Phys. Rev. Lett.*, 1974, **33**, 824.

17 R. Kostić and D. Stojanović, *Acta Phys. Pol. A*, 2009, **116**, 598.

18 Y. S. Peng, B. Xu, X. L. Ye, P. Jin, Z. G. Wang, *Microelectron. Eng.*, 2012, **93**, pp1–4.

19 S. H. Zhang, L. Wang, Z. W. Shi, Y. X. Cui, H. T. Tian, H. J. Gao, H. Q. Jia, W. X. Wang; H. Chen, L. C. Zhao, *Nanoscale Res. Lett.*, 2012, **7**, 87.

20 A. M Smith, S. Dave, S. Nie, L. True, and X. Gao, *Expert Rev. Mol. Dtagn.*, 2006, **6**, 231.

21 S. J. Cho, D. Maysinger, M. Jain, B. Röder, S. Hackbarth, and F. M. Winnik, *Langmuir*, 2007, **23**, 1974.

22 J. Y. Zhang, X. Y. Wang, and M. Xiao, *Opt. Lett.,* 2003, **28**, 1430.

23 A. P.Alivisatos, *Nat. Biotechnol.*, 2004, **22**, pp47-52.

24 Warren C. W. Chan，Dustin J. Maxwell，X. H. Gao, Robert E. Bailey, M. Y. Han, S. M. Nie, *Curr. Opin. Biotechnol.*, 2002, **13**, pp40-60.

25 Y. Song, S. W. Chen, *ACS Applied Materials & Interfaces*, 2014, DOI: 10.1021/am503388z.

26 A. L. Rogach, L. Katsikas, A. Kornowski, D. Su, A. Eychmüller, and H. Weller, *Ber Runsenges. Phys. Chem.*, 1996, **100**, 1772.

27 A. V. Nashchekin, K. G. Kolmakov, I. P. Soshnikov, N. M. Shmidt, and A. V. Loskutov, *Tech. Phys. Lett,.* 2003, **29**, 575.

28 A. L. Rogach, L. Katsikas, A. Kornowski, D. Su, A. Eychmüller, and H. Weller, *Ber Runsenges. Phys. Chem.,* 1997, **101**, 1668.

29 H. Zhang and B. Yang, *Thin Solid Films*, 2002, **418,** 169.

30 T. Inoshita, S. Ohnishi and A. Oshiyama, *Phys. Rev. Lett.*, 1986, **57,** 2560.

31 K. Y. Li, H. Zhang, W. Y. Yang, S. L. Wei, and D. Y. Wang, *Mate. Chem. Phys.*, 2010, **123**, 98.

32 K. Y. Li, G. J. Song, J. Zhang, C. M. Wang, and B. Guo, *J. Photochem. Photobiol. A*, 2011, **218**, 213.

33 H. Zhang, C. L. Wang, M. J. Li, X. L. Ji, J. H. Zhang, and B. Yang, *Chem. Mater.*, 2005, **17,** 4783.

34 M. Y. Gao, S. Kirstein, H. Mühwald, A. L. Rogach, A. Komowski, A. Eychmüller, and H. Weller, *J. Phys. Chem. B*, 1998, **102**, 8360.

35 L. Kronik and Y. Shapira, *Surf. Sci. Rep.*, 1999, **37,** 1.

36 A. Rosencwaig, *Science*, 1973, **181,** 657.

37 I. Mora-seró, S. Giménez, F. Fabregat-santiago, R. Gómez, Q. Shen, T. Toyoda, J. Bisquert, *Acc. Chem. Res.,* 2009, **42,** 1848-57.

38 S. Adachi, John Wiley & Sons Ltd Publication, New Jersey, 1nd edn., 2009, p168

39 T. Trindade, P. O'Brien, N. L. Pickett, *Chem. Mater.*, 2001, **13,** 3843-58.

40 D. Gal, J. Beier, E. Moons, G. Hodes, D. Cahen, L. Kronik, L. Burstein, B. Mishori, M. Leibovitch, Y. Shapira, D. Hariskos, R. Klenk, and H. W. Schock, *AIP Conf. Proc.*, 1996, **353,** 453.

41 S. Yuasa, T. Nagahama, and Y. Suzuki, *Science*, 2002, **297,** 234.

42 T. Niizeki, N. Tezuka, and K. Inomata, *Phys Rev Lett.*, 2008, **100,** 047207.

43 P. Harrison, John Wiley & Sons, Ltd, UK, 2nd edn., 2005, p285.

44 R. S. Quimby, M. G. Drexhage, and M. J. Suscavage, *Electron. Lett.*, 1987, **23**, 32

45 M. A. Stroscio and M. Dutta, Cambridge University press, UK, 1nd edn., 2001, pp131-167.

46 H. Zhang, Z. Zhou, and B. Yang, *J. Phys. Chem. B*, 2003, **107**, 8.

Nanoscale Accepted Manuscript